end of para.

particle beam therapy (PBT)

91   The technologies demonstrated in LhARA have the potential to be developed to make "best in class"
92   treatments available to the many. The laser-hybrid approach will allow radiobiological studies and eventually
93   radiotherapy to be carried out in completely new regimes, delivering a variety of ion species in a broad
94   range of time structures, spectral distributions, and spatial configurations at instantaneous dose rates up to
95   and potentially significantly beyond the current ultra-high dose-rate "FLASH" regime.

96   The LhARA consortium is the multidisciplinary collaboration of clinical oncologists, medical and
97   academic physicists, biologists, engineers, and industrialists required to deliver such a transformative
98   particle-beam system. With its "pre Conceptual Design Report" (pre-CDR) [The LhARA consortium
99   (2020)] the consortium lays out its concept for LhARA, its potential to serve a ground-breaking programme
100 of radiobiology, and the technological advances that will be made in its execution. The work presented in
101 the LhARA pre-CDR lays the foundations for the development of full conceptual and technical designs
102 for the facility. The pre-CDR also contains a description of the R&D that is required to demonstrate the
103 feasibility of critical components and systems. This paper presents a summary of the contents of the
104 pre-CDR and lays out the vision of the consortium.
105

2 MOTIVATION

106 RT delivered using protons and ions, particle-beam therapy (PBT), has the potential to overcome some
107 of the fundamental limitations of X-rays in cancer treatment through targeted delivery of the radiation
108 dose [Loeffler and Durante (2013)]. The Particle Therapy Co-Operative Group (PTCOG) currently lists
109 90 proton therapy facilities and 12 carbon ion therapy facilities, located predominantly in high-income
110 countries [PTCOG (2020)]. Low- and middle-income countries (LMIC) are relatively poorly served, indeed
111 nearly 70% of cancer patients globally do not have access to RT [Datta et al. (2019)] *Novel RT techniques*
112 incorporated in facilities that are robust, automated, efficient, and cost-effective are therefore required to
113 deliver the necessary scale-up in provision. This presents both a challenge and an opportunity; developing
114 the necessary techniques and scaling up RT provision will require significant investment but will also
115 create new markets, drive economic growth through new skills and technologies and deliver impact through
116 improvements in health and well-being. *(h published never?)*

117 **The case for a systematic study of the radiobiology of proton and ion beams**
118 The nature of the particle-tissue interaction confers on PBT the advantage that the dose can be precisely
119 controlled and closely conformed to the tumour volume. The efficacy of proton and ion beams is
120 characterised by their relative biological effectiveness (RBE) in comparison to reference photon beams.
121 The treatment-planning software that is in use in the clinic today assumes an RBE value for protons of
122 1.1 [Paganetti and van Luijk (2013)], meaning that a lower dose of protons is needed to produce the
123 same therapeutic effect that would be obtained using X-rays. However, the rapid rise in the linear energy
124 transfer (LET) at the Bragg peak leads to significant uncertainties in the RBE. Furthermore, it is known
125 that RBE depends strongly on many factors, including particle energy, dose, dose rate, the degree of
126 hypoxia, and tissue type [Paganetti (2014)]. A number of studies have shown that there can be significant
127 variation in RBE [Jones et al. (2018); Giovannini et al. (2016)]. Indeed, RBE values from 1.1 to over 3
128 have been derived from *in vitro* clonogenic-survival assay data following proton irradiation of cultured
129 cell lines derived from different tumours [Paganetti (2014); Chaudhary et al. (2014); Wilkens and Oelfke
130 (2004)]. RBE values of ~ 3 are accepted for high-LET carbon-ion irradiation, although higher values have
131 been reported [Karger and Peschke (2017)]. RBE uncertainties for carbon and other ion species are at
132 least as large as they are for protons. These uncertainties can lead to an incorrect estimation of the dose

complex end-points (e.g. angiogenesis and inflammation) in addition to routine survival measurements. The ability to evaluate charged particles in conjunction with other therapies (immunotherapy and chemotherapy), and of performing *in vivo* experiments with the appropriate animal models is a huge advantage given the current lack of evidence in these areas. LhARA therefore has the potential to ~~yield the accumulation~~ of radiobiological data that can ~~drive a significant change in current~~ clinical practice. The simulations of LhARA that are described in this document have been used to estimate the dose delivered as a function of energy for protons and carbon ions. Details of the simulations can be found in sections 3.3 and 3.4. The simulations show instantaneous particle rates of the order of 10^9 particles per shot can be achieved, corresponding to average dose rates up to $\gtrsim 120$ Gy/s for protons and $\gtrsim 700$ Gy/s for carbon ions. These estimates are based on the baseline specifications for LhARA.

Laser-hybrid beams for radiobiology and clinical application

High-power lasers have been proposed as an alternative to conventional proton and carbon-ion facilities for radiotherapy [Bulanov et al. (2002); Fourkal et al. (2003); Malka et al. (2004)]. The capability of laser-driven ion beams to generate protons and high-LET carbon ions at FLASH dose rates is a significant step forward for the provision of local tumour control whilst sparing normal tissue. High-power lasers have also been proposed to serve as the basis of electron, proton and ion-beams for radiobiology [Kraft et al. (2010); Fiorini et al. (2011); Doria et al. (2012); Zeil et al. (2013); Masood et al. (2014); Zlobinskaya et al. (2014)]. More recent projects (e.g. A-SAIL [A-SAIL Project (2020)], ELI [Cirrone et al. (2013)] and SCAPA [Wiggins et al. (2019)]) will also investigate radiobiological effects using laser-driven ion beams. These studies will also address various technological issues [Manti et al. (2017); Romano et al. (2016a); Masood et al. (2017); Chaudhary et al. (2017); Margarone et al. (2018)].

The LhARA collaboration's concept is to exploit a laser to drive the creation of a large flux of protons or light ions which are captured and formed into a beam by strong-focusing plasma lenses. Protons and ions at conventional facilities are captured at energies of several tens of keV. At such low energies the mutual repulsion of the particles, the "space-charge effect", limits the maximum instantaneous dose rate. The laser-driven source allows protons and ions to be captured at energies significantly above those that pertain in conventional facilities, thus evading the current space-charge limit on the instantaneous dose rate that can be delivered. Rapid acceleration will be performed using a fixed-field alternating-gradient accelerator (FFA) thereby preserving the unique flexibility in the time, energy, and spatial structure of the beam afforded by the laser-driven source. Modern lasers are capable of delivering a Joule of energy in pulses that are tens of femtoseconds in length at repetition rates of $\gtrsim 10$ Hz. At source, a laser-driven electron beam is reproducibly-well collimated and has a modest ($\sim 5\%$) energy spread. Laser-driven ion sources create beams that are highly divergent, have a large energy spread, and an intensity that can vary by up to 40% pulse-to-pulse. These issues are addressed in the conceptual design through the use of plasma lenses to provide strong focusing and to allow energy selection. In addition, sophisticated instrumentation will be used in a fast feedback-and-control system to ensure that the dose delivered is both accurate and reproducible. This approach will allow produce multiple ion species, from proton to carbon, to be produced from a single laser by varying the target foil and particle-capture optics.

The LhARA consortium's vision is that LhARA will prove the principle of the novel technologies required for the development of future therapy facilities. The legacy of the LhARA programme will therefore be:

- A unique facility dedicated to the development of a deep understanding of the radiobiology of proton and ion beams; and

Table 1. Design parameters of the components of the LhARA facility. The parameter table is provided in a number of sections. This section contains parameters for the Laser-driven proton and ion source, the Proton and ion capture section, and the Stage 1 beam transport section.

Parameter	Value or range	Unit
Laser driven proton and ion source		
Laser power	100	TW
Laser Energy	2.5	J
Laser pulse length	25	fs
Laser rep. rate	10	Hz
Required maximum proton energy	15	MeV
Proton and ion capture		
Beam divergence to be captured	50	mrad
Gabor lens effective length	0.857	m
Gabor lens length (end-flange to end-flange)	1.157	m
Gabor lens cathode radius	0.0365	m
Gabor lens maximum voltage	65	kV
Number of Gabor lenses	2	
Alternative technology: solenoid length	1.157	m
Alternative technology: solenoid max field strength	1.3	T
Stage 1 beam transport: matching & energy selection, beam delivery to low-energy end station		
Number of Gabor lenses	3	
Number of re–bunching cavities	2	
Number of collimators for energy selection	1	
Arc bending angle	90	Degrees
Number of bending magnets	2	
Number of quadrupoles in the arc	6	
Alternative technology: solenoid length	1.157	m
Alternative technology: solenoid max field strength (to serve the injection line to the Stage 2)	0.8 (1.4)	T

241 spreads, and reproducibility of such beams have meant that such sources are not suitable for a full
242 radiobiological laboratory setting. While a number of cell irradiation experiments have been conducted
243 with laser-accelerated ions [Doria et al. (2012); Zeil et al. (2013); Pommarel et al. (2017); Manti et al.
244 (2017)], these have been limited in scope to a single-shot configuration. In addition, most of these
245 experiments have been performed on high-power laser facilities with rapidly shifting priorities, where the
246 time to install dedicated diagnostic systems has not been available. A beam line to provide ion-driven
247 beams for multi-disciplinary applications, ELIMAIA (ELI Multidisciplinary Applications of laser-Ion
248 Acceleration) is being brought into operation at the Extreme Light Infrastructure (ELI) Cirrone et al. (2020);
249 Schillaci et al. (2019). This beam line will include the "ELI MEDical and multidisciplinary applications"
250 (ELIMED) beam line which will allow radiobiological investigations to be carried out Cirrone et al. (2016);
251 Romano et al. (2016b); Milluzzo et al. (2017); Pipek et al. (2017); Milluzzo et al. (2018); Cirrone et al.
252 (2020), ? LhARA is distinguished from this facility in that the energy at which the beam will be captured
253 has been chosen to maximise the shot-to-shot stability of the particle flux. As a result, LhARA has the
254 potential to become a unique, state-of-the-art system, able to explore the radiobiological benefits of a
255 laser-accelerated ion source.

256   A novel solution for ion-acceleration is to use a compact, flexible laser-driven source coupled to a
257 state-of-the-art beam-transport line. This allows an accelerating gradient of $\gtrsim 10\,\mathrm{GV/m}$ to be exploited at

258 the laser-driven source. We propose to operate in a laser-driven sheath-acceleration regime [Clark et al.
259 (2000a); Snavely et al. (2000); Daido et al. (2012)] for ion generation. An intense, short laser pulse will
260 be focused onto a target. The intense electric field generated on the front surface of the target accelerates
261 the surface electrons, driving them into the material. Electrons which gain sufficient energy traverse the
262 target, ionising the material as they go. A strong space-charge electric field, the 'sheath', is created as the
263 accelerated electrons exit the rear surface of the target. This field in turn accelerates surface-contaminant
264 ions. The sheath-acceleration scheme has been shown to produce ion energies greater than 40 MeV/u at the
265 highest laser intensities. The maximum proton energy (E_p) scales with laser intensity (I) as, $E_p \propto I^{\frac{1}{2}}$. The
266 laser required to deliver a significant proton flux at 15 MeV can be compact, relatively inexpensive, and is
267 commercially available.

268 The distribution of proton and ion energies observed in laser-driven beams exhibits a sharp cut off at
269 the maximum energy and, historically, the flux of laser-accelerated ion beams has varied significantly
270 shot-to-shot. To reduce the impact of the shot-to-shot variations, the choice has been made to select particles
271 from the plateau of the two-temperature energy spectrum of the laser-accelerated ion beam [Clark et al.
272 (2000b); Passoni et al. (2010).] This choice should enhance ion-beam stability and allow reproducible
273 measurements to be carried out at ultra-high dose rates using a small number of fractions. To create the flux
274 required in the plateau region, it is proposed that a 100 TW laser system is used. A number of commercial
275 lasers are available that are capable of delivering > 2.5 J in pulses of duration < 25 fs, at 10 Hz with
276 contrast better than $10^{10} : 1$. Shot-to-shot stability of $< 1\%$ is promised, an important feature for stable
277 ion-beam production.

278 Key to the operation of this configuration is a system that refreshes the target material at high-repetition
279 rate in a reproducible manner. A number of schemes have been proposed for such studies, from high-
280 pressure gases [Willingale et al. (2009); Bin et al. (2015); Chen et al. (2017)], cryogenic hydrogen ribbons
281 [Margarone et al. (2016); Gauthier et al. (2017); Obst et al. (2017)], liquid sheets [Morrison et al. (2018)]
282 and tape drives [Noaman-ul Haq et al. (2017)]. For the LhARA facility, a tape drive based on the system
283 developed at Imperial College London is proposed. This system is capable of reliable operation at target
284 thicknesses down to 5 μm, using both aluminium and steel foils, and down to 18 μm using plastic tapes.
285 Such tape-drive targets allow operation at high charge (up to 100 pC at 15 ± 1 MeV, i.e. $> 10^9$ protons per
286 shot) and of delivering high-quality proton and ion fluxes at repetition rates of up to 10 Hz or greater.

287 The careful control of the tension on the tape in a tape-drive target is critical for reproducible operation.
288 The tape must be stretched to flatten the surface, without stretching it to its plastic response. Surface
289 flatness is important for a number of reasons. Rippling of the front surface modifies the laser absorption
290 dramatically; uncharacterised rippling can make shot-to-shot variations significant and unpredictable
291 [Noaman-ul Haq et al. (2017)]. Similarly, rear surface perturbations can modify the sheath field, resulting
292 in spatial non-uniformities of the proton beam or suppression of the achievable peak energies. Tape drives
293 with torsion control and monitoring to maintain a high-quality tape surface have been designed and operated
294 in experiments at Imperial College London. The development of these targets continues with a view to the
295 production of new, thinner tapes for improved ion generation and the creation of ion species other than
296 proton and carbon. This is an active area of R&D that will continue with the development of LhARA.

297 High repetition-rate ion-beam diagnostics will also need to be developed. Such diagnostics will need to
298 measure both the energy spectrum and the spatial profile of the beams. Current methods are destructive and
299 are often limited to low-repetition rate. Passive detectors have not been demonstrated in the conditions that
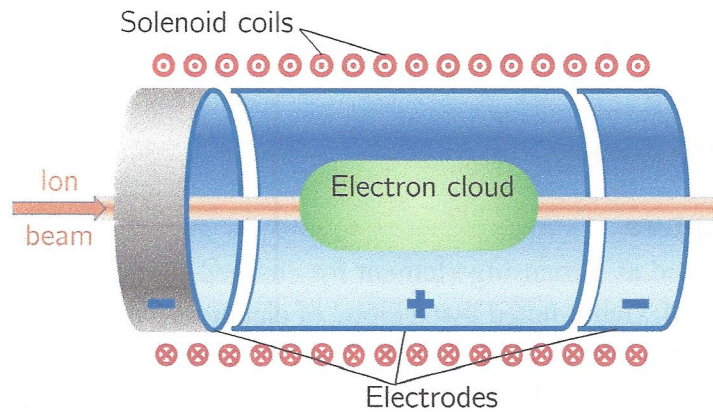300 will pertain at LhARA. Technologies being evaluated to address the issues raised by ion-source diagnostics

Figure 2. Schematic diagram of a Penning-Malmberg trap of the type proposed for use in the Gabor lenses to be used in LhARA. The solenoid coils, and the direction of current flow, are indicated by the red circles. The confining electrostatic potential is provided using a central cylindrical anode and two cylindrical negative end electrodes. The ion beam enters on-axis from the left and the electron cloud is indicated by the green shaded area.

332   Aslaninejad (2013)]:

$$B_{GPL} = B_{sol} \sqrt{Z \frac{m_e}{m_{ion}}} \; ; \tag{5}$$

333   where m_{ion} is the mass of the ions being focused, and Z is the charge state of the ions. In the case of a
334   proton beam the reduction factor is 43. Thus, for example, where a 2 T superconducting solenoid would be
335   required, the magnetic field required for a Gabor lens would only be 47 mT. This means the cost of the
336   solenoid for a Gabor lens can be significantly lower than the cost for a solenoid of equivalent focusing
337   strength.

Need to get to here.

338   The plasma-confinement system described above is commonly known as a 'Penning trap' and has found
339   wide application in many fields [Thompson (2015)]. Variations on the Penning trap where axial apertures
340   in the cathodes are introduced, such as the Penning-Malmberg trap [deGrassie and Malmberg (1980);
341   Malmberg et al. (1988)] are attractive for beam-based applications due to the excellent access provided to
342   the plasma column, see figure 2.

343   Instability of the electron cloud is a concern in the experimental operation of Gabor lens; azimuthal beam
344   disruption due to the diocotron instability has been observed and described theoretically [Meusel et al.
345   (2013)]. Theory indicates that the diocotron instability is most problematic under well-defined geometric
346   conditions. The reliable operation of a Gabor lens in a regime free from this instability has yet to be
347   demonstrated. Gabor lenses promise very strong focusing, simple construction, and low magnetic field,
348   all attractive features for LhARA. However, these attractive features come at the cost of relatively high
349   voltage operation ($\gtrsim 50\,\text{kV}$) and possible vulnerability to instability.

350   With reliable operation of Gabor lenses as yet unproven, we plan a two-part experimental and theoretical
351   programme of research to prove Gabor-lens suitability. Initial work will include: theoretical investigation
352   of lens stability in a full 3D particle-in-cell code such as VSIM [VSI (2020)]; and the development of
353   electron-density diagnostics based on interferometric measurement of the refractive-index change. These
354   activities will be applied to a time-invariant electron cloud. A test Gabor lens will be constructed to allow
355   validation of both the simulation results and a new diagnostic using an alpha emitter as a proxy for the
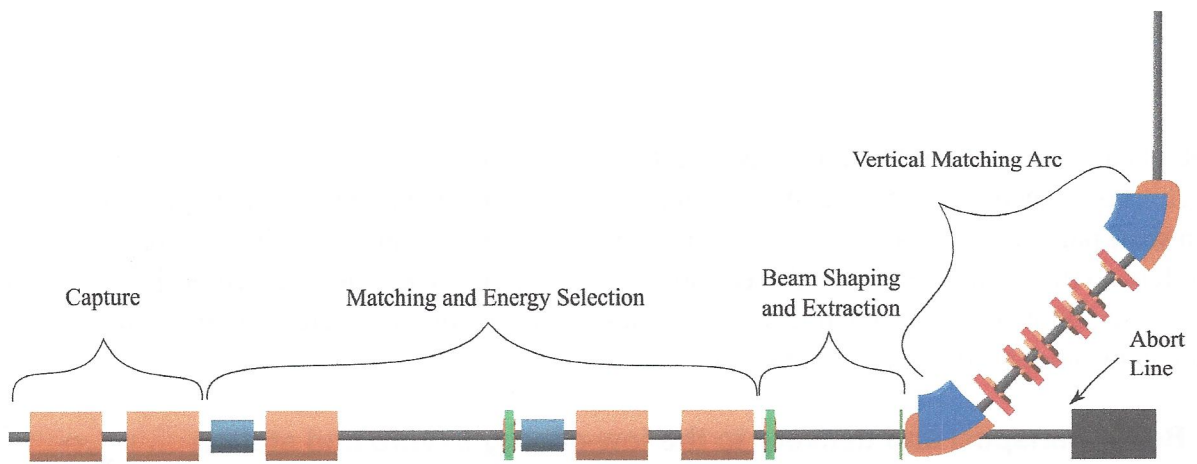
Figure 3. Beam transport for Stage 1 of LhARA visualised in BDSIM, showing five machine sections. The capture section is composed of two Gabor lenses (orange cylinders). The matching and energy selection section includes three Gabor lenses, two RF cavities (grey cylinders) and an octupole magnet (green disc). The beam shaping and extraction section includes a second octupole and a collimator (black vertical bar). The vertical matching arc directs the beam into the low-energy *in vitro* end station and is composed of two 45° dipoles and six quadrupoles. The total length of this beam line is 17.3 m.

400 resulting from octupolar focusing requires collimation to match the circular aperture through which the
401 beam enters the end station. A collimator is therefore positioned at the start of the vertical arc. Further
402 simulations are required to determine the optimum position of the second octupole and to evaluate the
403 performance of the octopoles. The switching dipole which directs the beam to the injection line of the FFA
404 in Stage 2 will be located between the second octupole and the collimator, requiring the octupole to be
405 ramped down for Stage 2 operation.

406   The vertical arc uses transparent optics in an achromat matching section to ensure that the first-order
407 transfer map through the arc is equivalent to the identity transformation and that any dispersive effects are
408 cancelled. A 2 m drift tube is added after the arc to penetrate the concrete shielding of the end station floor
409 and to bring the beam to bench height. The abort line consists of a drift followed by a beam dump and
410 requires the first vertical dipole to ramp down, preventing charged-particle transportation to the end station.

411   The underlying physics of plasma-lens operation cannot be simulated in BDSIM or GPT, however it
412 can be approximated using solenoid magnets of equivalent strength. RF cavity fields were not simulated.
413 10 000 particles were simulated corresponding to the estimated maximum bunch charge of 1×10^9 protons.
414 Figure 4 shows excellent agreement between horizontal and vertical transverse beam sizes in BDSIM
415 and MADX, verifying the beam line's performance in the absence of space-charge effects. Reasonable
416 agreement between BDSIM and GPT is also seen when space-charge forces are included in GPT. Emittance
417 growth is observed prior to the first solenoid, affecting the optical parameters throughout the machine.
418 However, the resulting beam dimensions at the cell layer of 1.38 cm horizontally and 1.47 cm vertically
419 are not significantly different from the ideal beam in BDSIM. Further adjustments of the Gabor lenses
420 and arc-quadrupole strengths may compensate for this. The transmission efficiency of the beam line is
421 approximately 100%.

422   The small bunch dimensions in both transverse planes at the focus after the third Gabor lens, where
423 the energy selection collimator will be placed, remains a concern if the effect of space-charge has been
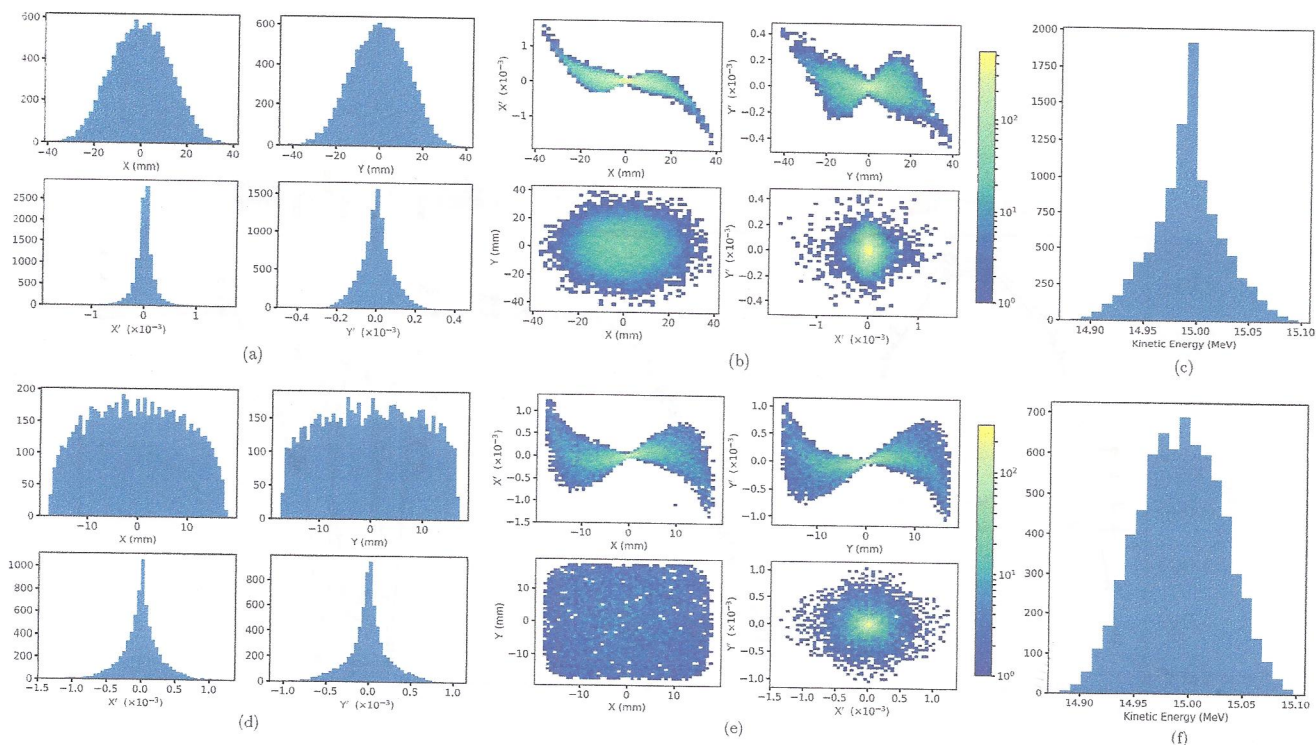
Figure 5. Beam phase space distributions at the end-station in the transverse plane, (X, Y); X′ and Y′ give the slope relative to the Z axis. The transverse phase space is shown in figures a and b for simulations without octupolar focusing and collimation, with the kinetic energy distribution shown in c. The same phase space distributions simulated with the effect of octupoles and collimation are in figures d, e, and f.

448 can be delivered with further optimisation of the octupoles and collimator.

449

450 ### 3.3.1 Alternative Design

451 To mitigate potential emittance growth from space-charge forces, an alternative beam line design was
452 developed in which the final two Gabor lenses in the matching and energy selection section are replaced by
453 four quadrupoles, limiting any bunch focusing to one plane at a time. The resulting machine is reduced
454 in length to 15.439 m. Without space-charge effects, a beam sigma of 2.5 mm at the end station can be
455 achieved. With space-charge, emittance growth prior to the first solenoid is once again observed leading
456 to an increased beam size at the entrance of the first quadrupole, resulting in a spatially asymmetric and
457 divergent beam at the end station. It is believed that the space-charge effects can be compensated by
458 applying the same Gabor-lens optimisation as in the baseline design and adjusting the quadrupole settings
459 to deliver beam parameters similar to those without achieved in the absence of space charge. The alternative
460 design provides a solution that is more resilient to space-charge effects than the baseline, however, only the
461 lower bound on the desired beam size has been achieved so far. Further optimisation is required not only to
462 optimise optical performance but also to optimise octupole settings and to determine whether a beam with
463 the desired uniformity can be delivered to the end station.

464

465 ## 3.4 Post-acceleration and beam delivery to the *in vitro* and *in vivo* end stations

466 A fixed-field alternating-gradient accelerator (FFA), based on the spiral scaling principle [Krest et al.
467 (1956); Symon et al. (1956); Fourrier et al. (2008); Tanigaki et al. (2006)], will be used to accelerate the
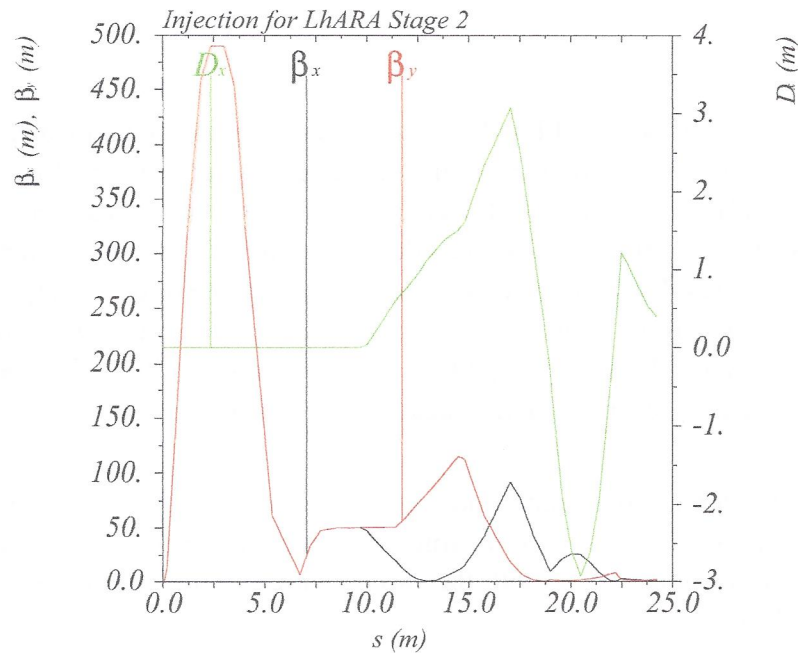468 beam in LhARA Stage 2 to obtain energies greater than the 15 MeV protons and 4 MeV/u carbon (C^{6+})

Figure 6. Twiss β_x and β_y functions and dispersion in the beam line consisting of the modified Stage 1 lattice and the transfer line allowing injection of the beam into the FFA ring. S goes from the laser target to the exit of the injection septum.

509   where B_0 is the magnetic field at radius R_0, k is the field index, ζ corresponds to the spiral angle and F
510   is the 'flutter function'. This field law defines a zero-chromaticity condition, which means the working
511   point of the machine is independent of energy up to field errors and alignment imperfections. This avoids
512   crossing any resonances, which would reduce the beam quality and may lead to beam loss.

513   Table 2 gives the main design parameters of the FFA ring. The ring consists of ten symmetric cells each
514   containing a single combined-function spiral magnet. The choice of the number of cells is a compromise
515   between the size of the orbit excursion, which dictates the radial extent of the magnet, and the length of the
516   straight sections required to accommodate the injection and extraction systems.

517   The betatron functions and dispersion in one lattice cell at injection are shown in figure 8a. The tune
518   diagram, showing the position of the working point of the machine in relation to the main resonance
519   lines, is shown in figure 8b. Tracking studies were performed using a step-wise tracking code in which the
520   magnetic field is integrated using a Runge-Kutta algorithm [Lagrange et al. (2018)]. The magnetic field in
521   the median plane was obtained using the ideal scaling law (equation 6) and using using Enge functions to
522   give the fringe fields. The field out of the median plane was obtained using Maxwell's equations and a
523   6th-order Taylor expansion of the field. The dynamic acceptance for 100 turns, shown for the horizontal
524   and vertical planes in figures 8c and 8d, respectively, are significantly larger than the beam emittance. This
525   statement holds even when the most pessimistic scenario, in which the emittance is assumed to be ten times
526   larger than nominal. These results confirm that a good machine working point has been chosen.

527   A full aperture, fast injection of the beam will be performed using a magnetic septum, installed on the
528   inside of the ring, followed by a kicker magnet situated in a consecutive lattice cell, as shown in figure 7.
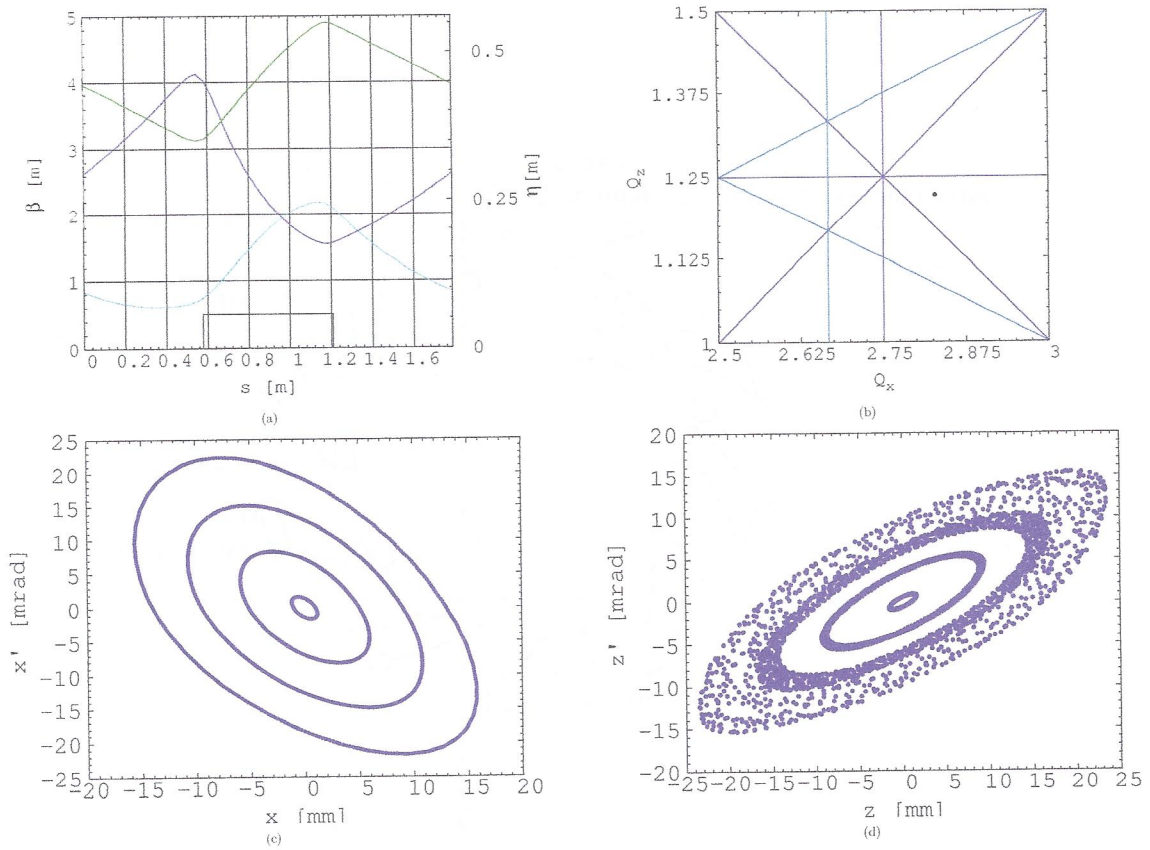
Figure 8. Beam optics and tracking in the FFA. Twiss β_h (blue), β_v (purple) functions and dispersion (green) in one lattice cell of the FFA ring (a). The working point of the FFA ring at (2.83, 1.22) on the tune diagram (b). The results of the horizontal (c) and vertical (d) dynamical acceptance study in the FFA ring, where a 1 mm offset is assumed in the vertical and horizontal planes respectively.

539 $\pm 0.7\%$ so a voltage of 4 kV is required to increase the energy acceptance to $\pm 2\%$. This voltage can be
540 achieved with one cavity [Yonemura et al. (2008)], two cavities are assumed to provide greater operational
541 stability. Normal conducting spiral-scaling FFA magnets, similar to the ones needed for LhARA, have
542 been constructed successfully [Tanigaki et al. (2006); Planche et al. (2009)] using either distributed,
543 individually-powered coils on a flat pole piece or using a conventional gap-shaping technique. For the
544 LhARA FFA, we propose a variation of the coil-dominated design recently proposed at the Rutherford
545 Appleton Laboratory in R&D studies for the upgrade of the ISIS neutron and muon source. In this case, the
546 nominal scaling field is achieved using a distribution of single-powered windings on a flat pole piece. The
547 parameter k can then be tuned using up to three additional independently-powered windings. The extent
548 of the fringe field across the radius of the magnet must be carefully controlled using a 'field clamp' to
549 achieve zero-chromaticity. An active clamp, in which additional windings are placed around one end of the
550 magnet, may be used to control the flutter function and thereby vary independently the vertical tune of the
551 FFA ring. The FFA is required to deliver beams over a range of energy; each energy requiring a particular
552 setting for the ring magnets. Therefore, a laminated magnet design may be required to reduce the time
553 required to change the field. The magnet gap of 4.7 cm given in table 2 is estimated assuming a flat-pole
554 design for the magnet. The details of the design will be addressed in as part of the LhARA R&D programme.
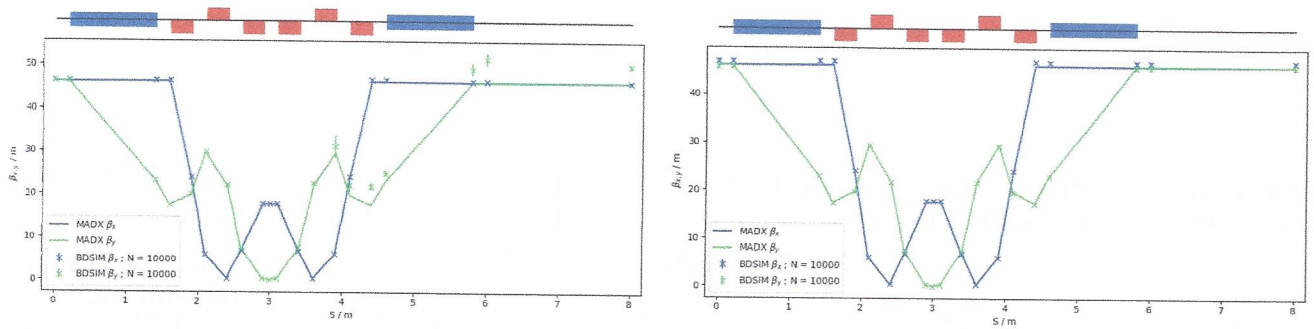555

Figure 9. Comparison of MAD-X and BDSIM simulation of 40 MeV (left) and nominal 127 MeV (right) proton beam passing through the high energy *in vitro* arc simulated with 10^4 particles (in BDSIM).

591   The quadrupole strengths for the scaled high-energy *in vitro* arc were obtained using MAD-X and
592   tracking simulations using BDSIM show good agreement, see figure 9. The input beam distribution used
593   in BDSIM was assumed to be Gaussian with Twiss $\beta = 46$, which gives a beam size of about 10 mm.
594   GPT simulations were performed which show small discrepancies due to space-charge effects. It may be
595   possible to compensate for this by adjusting the strengths of the quadrupoles in the arc and the matching
596   section in the extraction line.

597

598   ### 3.4.5 *In vivo* beam line

599   To facilitate efficient small-animal handling, an end station dedicated to *in vivo* experiments has been
600   positioned adjacent to the principle road access to the facility. If the first dipole of the high-energy *in vitro*
601   arc is not energised, the beam is sent to the *in vivo* end station. From the end of the extraction line, 7.7 m of
602   drift is necessary to clear the first bending dipole of the *in vitro* arc, to provide space for the five RF cavities
603   needed for longitudinal phase-space manipulation and to allow space for diagnostic devices. Following this
604   drift is a further 6.6 m of beam line that includes four quadrupoles, each of length 0.4 m, which are used to
605   perform the final focusing adjustments of the beam delivered to the *in vivo* end station. A final 1.5 m drift
606   at the end is reserved for scanning magnets to be installed to perform spot scanning and to penetrate the
607   shielding of the *in vivo* end station. In total, the *in vivo* beam line is 15.6 m in length.

608   The design is flexible in matching the various $\beta_{x,y}$ values given in table 4, but is not able to match
609   the smallest target value of $\beta_{x,y} = 0.039$ m for the pessimistic scenario, which is very challenging. To
610   verify that the optics design could provide the required beam sizes, simulations were performed with
611   BDSIM using an input Gaussian beam generated with the Twiss β values given in tables 4. Figure 10
612   shows the results of simulations for a 40 MeV proton beam and a nominal emittance 127 MeV proton
613   beam matched in order to obtain beam sizes of 1 mm, 10 mm and 30 mm. GPT was used to investigate the
614   effects of space-charge. These simulations show discrepancies compared to the BDSIM simulations. These
615   discrepancies can be compensated for by adjusting the strengths of the quadrupoles in the matching section
616   in the extraction line.

617

618   ## 3.5 Instrumentation

619   Commercial off-the-shelf (COTS) instrumentation will be used for Stages 1 and 2 of LhARA wherever
620   possible. However, the characteristics of the beam (e.g. very high charge-per-bunch, low-to-moderate
621   energy) will require some custom solutions to be developed. The authors are developing two concepts,
622   termed SciWire and SmartPhantom, for the low- and high-energy *in vitro* end stations respectively. These
623   detectors can also be used for beam diagnostics. This new instrumentation may find application at other

3.5.3 Beam line Instrumentation

The instrumentation requirement begins with the Ti:Sapphire laser. The laser focal spot will be characterised using a camera-based system and high-speed wavefront measurements [Wang (2014)] from COTS vendors.

For the Stage 1 beam line, beam position monitors (BPMs) will be needed for beam steering. Because of the low beam energy, non-intercepting BPMs using capacitive pickup buttons will be used. Custom pickups will be needed to match the beam pipe geometry but COTS electronics are available. The beam current will be monitored near the end of each beam line, using integrating current toroids (ICT), backed up with the option of insertable multi-layer Faraday cups (MLFC) to give absolute beam current and energy measurements. Beam profiles could be measured by SEM grids on both Stage 1 and Stage 2 beam lines. For Stage 1, these monitors will be mounted on pneumatic actuators to avoid scattering. Each end station could be equipped with insertable "pepper-pot" emittance monitors and a transverse deflection cavity with fluorescent screen could be provided for bunch shape measurements.

The BPMs on the FFA will require pickup designs suitable for the unusual, wide and shallow vacuum vessel. The FFA at the KURNS facility in Kyoto is of a similar layout [Uesugi (2018)] and uses a kicker and capacitive pickup to perform tune measurements in each transverse direction. A minimum of one BPM every second cell will be used in the FFA so that the beam orbit can be measured. BPMs will also be required close to the injection and extraction septa. The BPM system may be able to use COTS electronics, but the pickups will be based on the KURNS design of multiple electrodes arranged across the vacuum vessel width.

The data acquisition system needs to be able to store calibration data and apply corrections in real time. It is necessary to be able to find the beam centre from a profile, even when the profile may be non-Gaussian and possibly asymmetric. Field programmable gate arrays (FPGAs) can be used to perform fast fitting and pattern recognition of beam profiles. The instrumentation will be integrated with the accelerator control system to be able to provide fast feedback and adjustment of the beam parameters in real time.

3.6 Biological end stations

In order to deliver a successful radiobiological research programme, high-end and fully equipped *in vitro* and *in vivo* end-stations will be housed within the LhARA facility. The two *in vitro* end-stations (high and low energy) will contain vertically-delivered beam lines which will be used for the irradiation of 2D monolayer and 3D-cell systems (spheroids and patient-derived organoids) in culture. The beam line within the end-stations will be housed in sealed units that will be directly sourced with appropriate gases (carbon dioxide and nitrogen), allowing for the cells within culture plates to be incubated for a short time in stable conditions prior to and during irradiation. This will also enable the chamber to act, where necessary, as a hypoxia unit (0.1%–5% oxygen concentration). Furthermore, these sealed units will contain robotics to enable simple movement of the numerous cell culture plates housed within to be placed into and taken away from the beam.

The *in vitro* end-stations will be located within a research laboratory equipped with up-to-date and state-of-the-art facilities. The laboratory will include all the vital equipment for bench-top science, sample processing and analysis (e.g. refrigerated centrifuges and light/fluorescent microscopes), along with the equipment required for contaminant-free cell culture (e.g. humidified CO_2 cell culture incubators, Class II biological safety cabinets), and for the storage of biological samples and specimens (e.g. $-20°C$ and $-80°C$ freezers and fridges). The laboratory will also house an X-ray irradiator (allowing direct RBE comparisons between conventional photon irradiation, and the proton and carbon ions delivered by the accelerator),

736 For a facility such as LhARA, radiation safety is a primary concern and all work will be completed
737 under Regulation 8 of the Ionising Radiations Regulations 2017 (IRR17) [HSE (2018)], which requires a
738 radiation risk assessment before commencing a new work activity involving ionising radiation.

739 The infrastructure and integration of the LhARA facility will require R&D in four key areas: risk analysis
740 (project risks), risk assessments (safety risks), radiation simulations, and controls development. The risk
741 analysis will cover all aspects of the facility, such as funding and resource availability, not just technical
742 risks. A safety-risk assessment will be performed to describe and control all potential safety risks in the
743 facility. The safety-risk assessment will, to a reasonable degree, identify all pieces of equipment that
744 require safety mitigations and identify control measures that must be put in place. Coupled closely with the
745 safety-risk assessment, radiation simulations will be developed to characterise the radiation hazards in and
746 around the LhARA facility. The last area to require R&D will be the control systems. It is expected that the
747 facility will use the Experimental Physics and Industrial Control System (EPICS), which can be further
748 developed at this stage.
749

4 PERFORMANCE

750 The dose distributions delivered to the end stations were evaluated using BDSIM. Figure 11 shows the
751 energy lost by the beam as it enters the low-energy *in vitro* end station. The beam passes through the
752 vacuum window, a layer of scintillating fibre, and a 5 mm air gap. The beam then enters the cell-sample
753 container, assumed to be polystyrene, which supports a $30\,\mu m$ thick layer of cells, modelled using the
754 Geant4 material "G4_SKIN_ICRP" [NIST (2017)]. The transverse momentum of protons in the beam was
755 assumed to be Gaussian distributed, with a lateral spread small enough for the beam to be fully contained
756 within the required spot size of 3 cm. Figure 11 shows that a proton beam with 10 MeV kinetic energy
757 does not reach the cell. The Bragg peak of a 12 MeV proton beam is located close to the cell layer, while
758 a 15 MeV beam, the maximum energy specified for delivery to the low-energy *in vitro* end station, has
759 a Bragg peak located beyond the cell layer. LhARA's ability to deliver various energies will allow the
760 investigation of radiobiological effects for irradiations using different parts of the Bragg peak, effectively
761 varying the LET across the sample.

762 The maximum dose that can be delivered was evaluated for a variety of beam energies. In order for the
763 dose to be reported in units of Gray it is necessary to define the volume within which the energy deposition
764 is to be integrated. Therefore, the dose was estimated from simulations by calculating the energy deposited
765 in a volume of water corresponding in size to the sensitive volume of a PTW 23343 Markus ion chamber
766 [PTW (2019/2020)] placed at the position of the Bragg peak in each case. This choice allows the doses and
767 dose-rates reported below to be compared to other facilities which are in operation since the PTW 23343
768 Markus ion chamber is widely at existing facilities. The cylindrical sensitive volume of the ion chamber
769 has a radius of 2.65 mm and a depth of 2 mm, giving a volume of about 4.4×10^{-8} m^3. The total energy
770 deposited within the chamber was recorded and converted into dose in units of Gray.

771 For the low-energy *in vitro* end station, the minimum spot size is specified to have a diameter of 10 mm,
772 which is larger than the area of the chamber. A single shot of 10^9 protons at 12 MeV with the minimum
773 design spot size deposits 3.1×10^{-4} J in the chamber volume, corresponding to a dose of 7.1 Gy. For this
774 simulation, the thickness of the sample container was reduced so that the Bragg peak could be positioned
775 within the chamber volume. For the bunch length of 7.0 ns, the maximum instantaneous dose rate is
776 1.0×10^9 Gy/s and the average dose rate is 71 Gy/s, assuming a repetition rate of 10 Hz. A single shot of
777 10^9 protons at 15 MeV deposits 5.6×10^{-4} J in the chamber volume, corresponding to a dose of 12.8 Gy.

Table 5. Summary of expected maximum dose per pulse and dose rates that LhARA can deliver for minimum beam sizes. These estimates are based on Monte Carlo simulations using a bunch length of 7 ns for 12 MeV and 15 MeV proton beams, 41.5 ns for the 127 MeV proton beam and 75.2 ns for the 33.4 MeV/u carbon beam. The average dose rate is based on the 10 Hz repetition rate of the laser source.

	12 MeV Protons	15 MeV Protons	127 MeV Protons	33.4 MeV/u Carbon
Dose per pulse	7.1 Gy	12.8 Gy	15.6 Gy	73.0 Gy
Instantaneous dose rate	1.0×10^9 Gy/s	1.8×10^9 Gy/s	3.8×10^8 Gy/s	9.7×10^8 Gy/s
Average dose rate	71 Gy/s	128 Gy/s	156 Gy/s	730 Gy/s

proton beam and 33.4 MeV/u carbon-ion beam simulations.

5 CONCLUSIONS

The initial conceptual design of LhARA, the Laser-hybrid Accelerator for Radiobiological Applications, has been described and its performance evaluated in simulations that take into account the key features of the facility. LhARA combines a laser-driven source to create a large flux of protons or light ions which are captured and formed into a beam by strong-focusing plasma lenses thus evading the current space-charge limit on the instantaneous dose rate that can be delivered. Acceleration, performed using a fixed-field alternating-gradient accelerator, preserves the unique flexibility in the time, spectral, and spatial structure of the beam afforded by the laser-driven source. The ability to trigger the laser pulse that initiates the production of protons or ions at LhARA will allow the time structure of the beam to be varied to interrupt the chemical and biological pathways that determine the biological response to ionising radiation. In addition, the almost parallel beam that LhARA will deliver can be varied to illuminate a circular area with a maximum diameter of between 1 cm and 3 cm with an almost uniform dose or focused to a spot with diameter of $\sim$ 1 mm. These features make LhARA an extremely flexible tool for the systematic study of the radiobiology of proton and ion beams.

The laser-hybrid approach, therefore, will allow radiobiological studies and eventually radiotherapy to be carried out in completely new regimes, delivering a variety of ion species in a broad range of time structures and spatial configurations at instantaneous dose rates up to and potentially significantly beyond the current ultra-high dose-rate "FLASH" regime. By demonstrating a triggerable system that incorporates dose-deposition imaging in the fast feedback-and-control system, LhARA has the potential to lay the foundations for "best in class" treatments to be made available to the many by reducing the footprint of future particle-beam therapy systems.

LhARA has the potential to drive a change in clinical practice in the medium term by increasing the wealth of radiobiological knowledge. This enhanced understanding in turn may be used to devise new approaches to decrease radio-toxicity on normal tissue while maintaining, or even enhancing, the tumour-control probability. The radiobiology programme in combination with the demonstration in operation of the laser-hybrid technique means that the execution of the LhARA programme has the potential to drive a step-change in the clinical practice of proton- and ion-beam therapy.

ACKNOWLEDGEMENTS